High-pressure deformation mechanism in scolecite: A combined computational-experimental study

PIETRO BALLONE,[1] SIMONA QUARTIERI,[2] ALESSANDRA SANI,[3] AND GIOVANNA VEZZALINI[4,*]

[1]Dipartimento di Fisica and INFM, Salita Sperone 31, I-98166 Messina-S.Agata, Italy
[2]Dipartimento di Scienze della Terra, Salita Sperone 31, I-98166 Messina-S.Agata, Italy
[3]European Synchrotron Radiation Facility, BP 220, F-38042 Grenoble Cedex, France
[4]Dipartimento di Scienze della Terra, Largo S. Eufemia, 19, I-41100 Modena, Italy

ABSTRACT

Pressure-induced structural modifications in scolecite were studied by means of in situ synchrotron X-ray powder diffraction and density functional computations. The experimental cell parameters were refined up to 8.5 GPa. Discontinuities in the slope of the unit-cell parameters vs. pressure dependence were observed; as a consequence, an increase in the slope of the linear pressure-volume dependence is observed at about 6 GPa, suggesting an enhanced compressibility at higher pressures. Weakening and broadening of the diffraction peaks reveals increasing structural disorder with pressure, preventing refinement of the lattice parameters above 8.5 GPa. Diffraction patterns collected during decompression show that the disorder is irreversible. Atomic coordinates within unit cells of different dimensions were determined by means of Car-Parrinello simulations. The discontinuous rise in compressibility at about 6 GPa is reproduced by the computation, allowing us to attribute it to re-organization of the hydrogen bonding network, with the formation of water dimers. Moreover we found that, with increasing pressure, the tetrahedral chains parallel to *c* rotate along their elongation axis and display an increasing twisting along a direction perpendicular to *c*. At the same time, we observed the compression of the channels. We discuss the modification of the Ca polyhedra under pressure, and the increase in coordination number (from 4 to 5) of one of the two Al atoms, resulting from the approach of a water molecule. We speculate that this last transformation triggers the irreversible disordering of the system.

INTRODUCTION

Zeolites are low-density silicates that occur as minerals, but are also important synthetic materials. They are used as catalysts, selective sorbers, and ionic exchangers. These applications are based on their structure, which consists of an aluminosilicate framework with cavities and channels of various sizes and hosts cations and water molecules.

Industrial applications of zeolites depend on their thermal stability and temperature-induced phase transformations, which consequently have been the subject of extensive and systematic investigations (Bish 1995; Alberti and Vezzalini 1984). On the other hand, the effect of pressure on these framework silicates has been largely neglected up to now, and only a few quantitative determinations of the cell parameters, crystal structure, and properties of pressure-induced polymorphic phases have been reported in the literature (Hazen and Finger 1979, 1984; Velde and Besson 1981; Hazen 1983; Belitsky et al. 1992; Gillet et al. 1996; Goryainov et al. 1996, 1999; Huang 1998; Bazhan et al. 1999; Secco and Huang 1999; Comodi et al. 2001;

Lee et al. 2002; Vezzalini et al. 2001). It is nevertheless apparent that pressure can induce important structural changes and profound modifications in the physical properties of zeolites that, in turn, could result in new specific applications. At lower pressure these effects result mainly from the deformation of the cavities or from the rearrangement and enhanced mobility of the extra-framework species. The presence in zeolites of open cavities and channels allows the detailed study of these effects using both penetrating and non-penetrating pressure-transmitting media, as shown in previous studies of structural effects of pressure on natrolite and edingtonite (Belitsky et al. 1992) and on zeolite A (Hazen and Finger 1984). At high pressure (H*P*), the compression of these micro-porous materials often induces disorder in the framework structure, and it has been shown that structural order can be partially (hydrated zeolite Na-A: Secco and Huang 1999) or completely (heulandite: Vezzalini et al. 2001; Na-Y and Li-A: Huang 1998) recovered on the release of pressure, or completely lost (wairakite: Goryainov et al. 1996, 1999). The relevance of these effects for industrial applications has been demonstrated by Secco and Huang (1999) for zeolite Na-A, in which the progressive structural disordering under pressure (up to 1.8 GPa) gives rise to an anomalous increase of the ionic conductivity. The residual

---

disorder in the partially recovered sample confers new transport properties on Na-A zeolite.

Scolecite is a calcium zeolite with NAT topology (Meier et al. 1996) and an ordered (Si, Al) distribution. The main features of its structure are well known (see, for example, Fälth and Hansen 1979; Kvick et al. 1985; Stuckenschmidt et al. 1997): chains parallel to **c** are composed of 4-membered rings of tetrahedra in which opposing tetrahedra are joined by a fifth one. The connection of the chains gives rise to a three dimensional framework and also defines a well ordered network of channels. In the zeolites of this group, each channel parallel to **c** contains four extra-framework sites. In scolecite, one site is occupied by Ca and the other three are occupied by water molecules (Figs. 1a and 1b).

The progressive pressure-induced amorphization of scolecite was studied by Gillet et al. (1996) by means of in situ X-ray diffraction in energy-dispersive mode and Raman spectroscopy. The experimental data show progressive structural changes below 10 GPa, and show that the crystal to amorphous phase change is irreversible. Moreover, pressure-enhanced molecular self-diffusion in zeolites with the NAT topology was recently studied by Moroz et al. (2001).

In the present study, a combined experimental (in situ synchrotron X-ray powder diffraction) and computational (density functional theory, DF) approach is used to determine the dependence of the lattice parameters on pressure, and to identify the atomistic mechanisms underlying the structural changes and phase transformations of scolecite under pressure. In this respect, the experimental and computational techniques we use complement each other in the most favorable way, since lattice parameters and phase boundaries are determined by the experimental measurements, while DF is used as a flexible tool to model the structural changes in the zeolites under pressure and to analyze them with atomistic resolution.

Our interest in scolecite for these HP studies is motivated by the results of Gillet et al. (1996) mentioned above, and by the fact that the deformation mechanisms induced by dehydration of scolecite (Ståhl and Hanson 1994), and other zeolites

with NAT topology (Alberti and Vezzalini, 1983; Baur and Joswig, 1996; Joswig and Baur 1995) are well known, and provide both a benchmark and a guideline for the interpretation of the HP results. An additional and important reason for selecting scolecite is that its structure is relatively simple, with an ordered distribution of Si, Al, and extra-framework species. Hence, it is possible to model the HP behavior of scolecite by refined computational methods.

EXPERIMENTAL METHODS

The scolecite sample used in this study ($Na_{0.32}Ca_{7.71}Al_{15.60}Si_{24.36}O_{80} \cdot 26.51H_2O$) is from Teigarhorn (Berufjördur, Iceland). The cell parameters at room P and T were $a = 18.513(2)$, $b = 19.000(2)$, $c = 6.528(1)$ Å and $\beta = 90.629(6)°$. The non standard monoclinic $F1d1$ space group is assumed here for better comparison with the structure of natrolite (space group $Fdd2$).

The powder diffraction experiments were performed at the ID09 beamline of the ESRF (European Synchrotron Radiation Facilities), at a fixed wavelength of 0.4103 Å. The high pressure experiments were carried out by placing the powdered zeolite samples in the gasket hole of a 600 μm diameter diamond anvil cell, using silicon oil as a non-penetrating pressure-transmitting medium (Gillet et al. 1996). A known problem in deriving by the use of non-penetrating media is their limited range of hydrostaticity. The hydrostaticity of silicon oil can be considered satisfactory up to at least 5 GPa, on the basis of the good agreement between the results obtained from the zeolite heulandite using glycerol (Comodi et al. 2001) and silicon oil (Vezzalini et al. 2001). Moreover, Le Bihan et al. (1996) studied several intermetallic uranium compounds under high pressure with different pressure-transmitting media (silicon oil, ethanol-methanol-water, and liquid argon). Stress due to the solidification of silicon oil was observed at about 9 GPa; however, at lower pressure no significant difference was observed with respect to the other pressure transmitting media. The pressure values were determined from the shift of the fluorescence line of ruby, excited by means of an Ar laser, and adopting the non-linear hydrostatic pressure scale (Mao et al. 1986). The estimated error in the pressure values is 0.1 GPa, both on the basis of previous calibrations, and by comparing the pressure oscillations before and after each data collection. The experiments were performed up to 11 GPa and some pressure points were also collected during decompression of the sample. An MAR345 imaging plate detector (pixel dimension 100 μm) was used. The sample was rocked by ±3° in ϖ to reduce texture in the diffraction images. Exposure times were 32–33 sec, and the sample to detector distance was 367 mm. One-dimensional ($2\theta_{max} = 25°$) diffraction patterns were obtained by integrating the two-dimensional images using the program FIT2D (Hammersley et al. 1996). The size of the X-ray beam, focused vertically by means of a Pt-coated Si-mirror and horizontally by means of an asymmetrically cut Si (111) monochromator (Schulze et al. 1998), was 30×30 μm^2.

The unit-cell parameters were refined using the GSAS package of programs (Larson and Von Dreele 1994). The coordinates of the $F1d1$ structure proposed by Stuckenschmidt et al. (1997) were used as the starting set. The background curve was fitted with a Chebyshev polynomial with 24 coefficients.
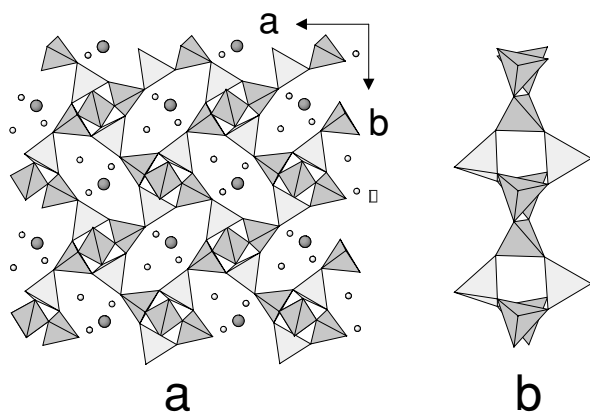

FIGURE 1. Scolecite at room pressure: (**a**) view of the structure in the *a-b* plane; (**b**) tetrahedral chain running parallel to *c*.

The pseudo-Voigt profile function proposed by Thomson et al. (1987), with the asymmetry correction from Finger et al. (1994), was used to fit the experimental pattern. For each of the samples, the scale factor and background were refined first, then the cell parameters, and finally the Gaussian (GW) and the Lorentzian (LX) profile parameters. The values obtained by the Le Bail method (Le Bail et al. 1988), using the same profile function and following the same refinement strategy, were similar to those obtained by means of the Rietveld refinement. Refinement of the unit-cell parameters for the powder patterns collected in the range $P_{amb} - 4.0$ GPa was performed up to $2\theta = 20°$, while for those collected in the P range 5.1–8.5 GPa the refinement was performed up to $2\theta = 15°$. The resulting values are reported in Table 1.

COMPUTATIONAL METHOD

The computational technique that we applied is described in several publications (e.g., Galli and Parrinello 1991; Marx and Hutter 2000). Here we provide the necessary details for an informed reader to reproduce our data. Computations were performed within the DF framework, with a recent gradient-corrected approximation for the exchange and correlation energy (Perdew et al. 1996). This functional is known to reliably describe both the strong ionic-covalent bonds in the alumino-silicate framework (Hamann 1996) and the relatively weak hydrogen bonds of the intra-channel water molecules (Hamann 1997). Only valence electrons were included in the computation, and their interaction with the ionic cores was described by soft norm-conserving pseudopotentials (Troullier and Martins 1991). The radii and the atomic configurations used in the pseudopotential generation are listed in Table 2. The independent electron orbitals (Kohn-Sham orbitals) were expanded on the basis of plane waves, with a kinetic energy limit of 100 Ry. The corresponding limit for the valence electron density was 400 Ry, which resulted in a Fourier representation with more than one million plane waves. The reason for such a high limit is briefly discussed below. At fixed atomic geometry, determination of the Kohn-Sham orbitals is performed by direct minimization of the total energy functional (Hutter et al. 1994).

TABLE 1. Experimental unit-cell parameters from powder patterns and ψ angles calculated at different pressures

P (GPa)	a (Å)	b (Å)	c (Å)	β (°)	V (Å³)	ψ *cell (Å)
0	18.513(2)	19.000(2)	6.528(1)	90.629(6)	2296.1(3)	22.6
0.4	18.469(1)	18.951(2)	6.519(1)	90.550(7)	2281.7(2)	23.0
0.7	18.426(2)	18.908(1)	6.508(1)	90.511(6)	2267.3(2)	23.3
0.9	18.421(1)	18.917(2)	6.509(1)	90.469(6)	2268.2(2)	23.3
1.2	18.370(2)	18.871(2)	6.496(1)	90.450(7)	2251.8(2)	23.6
1.6	18.339(2)	18.832(1)	6.489(1)	90.362(7)	2242.0(2)	23.9
1.9	18.301(2)	18.821(2)	6.481(1)	90.366(7)	2232.3(3)	24.0
2.2	18.272(2)	18.800(2)	6.473(1)	90.338(7)	2223.7(3)	24.2
2.5	18.268(1)	18.788(1)	6.471(1)	90.271(4)	2221.2(2)	24.3
2.7	18.220(2)	18.757(2)	6.460(1)	90.269(6)	2207.6(3)	24.5
3.1	18.211(1)	18.732(1)	6.460(1)	90.051(6)	2203.7(2)	24.6
3.6	18.170(1)	18.700(1)	6.448(1)	90.027(5)	2191.1(2)	24.9
4.0	18.132(1)	18.672(1)	6.437(1)	90.011(5)	2179.4(2)	25.1
5.1	18.037(4)	18.619(4)	6.416(1)	89.91(2)	2154.7(5)	25.7
6.6	17.879(7)	18.367(8)	6.413(2)	89.85(4)	2102.6(9)	27.1
7.5	17.760(7)	18.038(7)	6.414(2)	89.72(4)	2054.8(8)	28.3
8.5	17.593(8)	17.722(8)	6.407(2)	88.95(5)	1997.4(8)	29.8

* Calculated, after Alberti and Vezzalini (1981), from the values of the experimental cell parameters.

TABLE 2. Atomic configuration and cut-off radii used for the generation of the non-local, norm conserving pseudo potentials used in the present computations (see Troulier and Martins 1991 for details of the generation procedures)

Element	Angular momentum	Valence configuration	r_c (a.u.)
H	s	s^1	0.5
O	s	$s^2 p^4$	1.4
	p	$s^2 p^4$	1.4
Al	s	$s^2 p^1$	1.6
	p	$s^2 p^1$	1.7
	d	$s^1 p^{0.75} d^{0.25}$	1.7
Si	s	$s^2 p^2$	1.4
	p	$s^2 p^2$	1.4
	d	$s^2 p^{0.75} d^{0.25}$	1.4
Ca	s	s^2	2.1
	p	$s^1 p^{0.5}$	2.5

Because of the large volume of the unit cell, the sampling of the Brillouin zone is limited to the Γ point only. The gradient of the total energy with respect to the ionic positions is computed, and the ionic configuration is optimized by molecular dynamics (MD) for fixed shape and size of the unit cell, following the method of Car and Parrinello (1985). The relaxation is achieved by slowly decreasing the kinetic energy of the ions and is terminated when the largest force on the atoms is below 0.5×10^{-3} atomic units.

Computations of this type are known to provide the most efficient and reliable tool for investigating structural properties of systems consisting of many (up to a few hundred) inequivalent atoms. Nevertheless, slight errors are introduced by the exchange-correlation energy approximation and the pseudopotential approximation. These errors, which are often systematic, need to be taken into account when comparing the results of experiments and DF computations. At equal pressure, computed and measured lattice constants often differ by ~1–2% for systems such as Si or SiO_2, or, analogously, the pressure corresponding to equal lattice constants may differ by a few 10^{-1} GPa. It is important to note that these estimates of errors are valid for relatively simple systems, while no systematic and fully quantitative assessment of the reliability of DF is available for complex solids like scolecite, or for systems undergoing structural phase transitions. It is also important to emphasize that the investigation of the pressure dependence of the scolecite structure remains a very demanding task, because of the large size (200 atoms) of the unit cell, the number of independent lattice parameters (four), and especially because of the sensitivity of the pressure estimation on the quality (size) of the plane wave basis set. For all these reasons, we adopted a limit much greater than required for determination of the atomic positions in a fixed unit cell, and in comparing our computational results with the experimental data we did not rely on the precise determination of the lattice parameters as a function of pressure. Instead, we varied these parameters in a range suggested by the experimental data, and estimated the pressure *a posteriori* on the basis of a sequence of total energy computations at different volumes. The corresponding evolution of the

relaxed atomic position with changing lattice parameters provides valuable information about the atomistic mechanisms underlying the scolecite properties under pressure.

The DF scheme outlined above was used to determine the equilibrium atomic positions and the total energy for the unit cell of scolecite with lattice parameters listed in Table 3. At the experimental ambient-pressure volume, the computation was performed using the atomic coordinates from Stuckenschmidt et al. (1997) as the initial configuration. For each of the other volumes computations were begun from the relaxed positions for the closest volume already computed, rescaled according to the ratio of the lattice parameters. No symmetry restriction was applied during the relaxation of the atomic positions, in order to allow the system to decrease its energy by reducing its symmetry under applied pressure. Moreover, the water content of untreated scolecite was maintained, since no sign of dehydration was observed in previous HP studies of zeolites (Gillet et al. 1996; Comodi et al. 2001).

EXPERIMENTAL RESULTS

A scolecite X-ray powder diffraction pattern collected at room pressure on the MAR345 image plate detector is shown in Figure 2. The peculiar feature of this image, also observed in all the patterns collected at high pressure, is the presence of many spots caused by the poor statistics of the diffraction data, due to the low mosaicity of the crystallites and the small volume irradiated by the beam. These factors, together with the development of strong preferred orientations in the compressed powder, prevent correct measurement of the diffraction intensities. Hence, only the unit-cell parameters were extracted from the powder patterns.

Figure 3 shows that the peak intensities decrease and the peak profiles become broader with increasing pressure. In particular, the presence at high pressure of very broad and weak peaks limited refinement of the cell parameters to the data collected up to 8.5 GPa. While Gillet et al. (1996) report the presence of new diffraction peaks in the scolecite patterns above 6 GPa, in our experiment we did not observe the appearance of new peaks.

As shown in Table 1 and Figure 4, the contraction of the cell parameters in the range 0–8.5 GPa is approximately 5.0, 7.0, 2.0, and 2% for a, b, c, and β respectively, and the volume
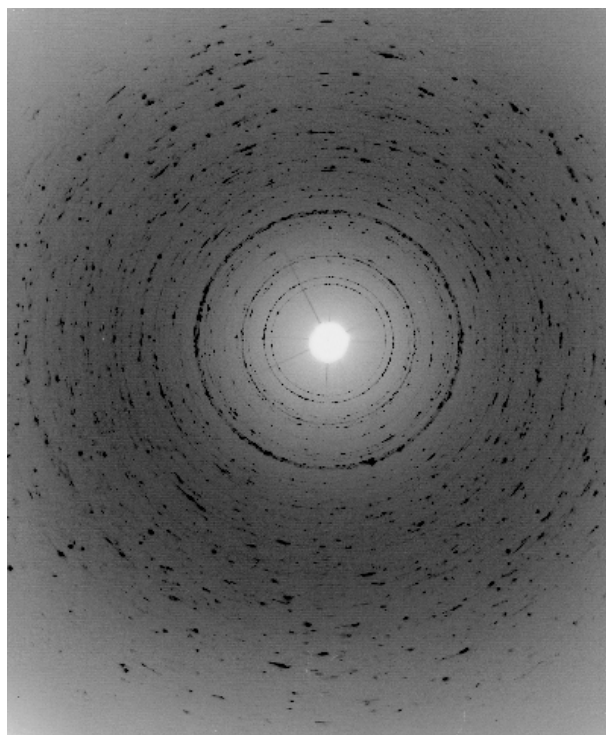

FIGURE 2. Powder X-ray diffraction pattern of scolecite in DAC obtained with MAR345 image plate detector at ambient pressure.
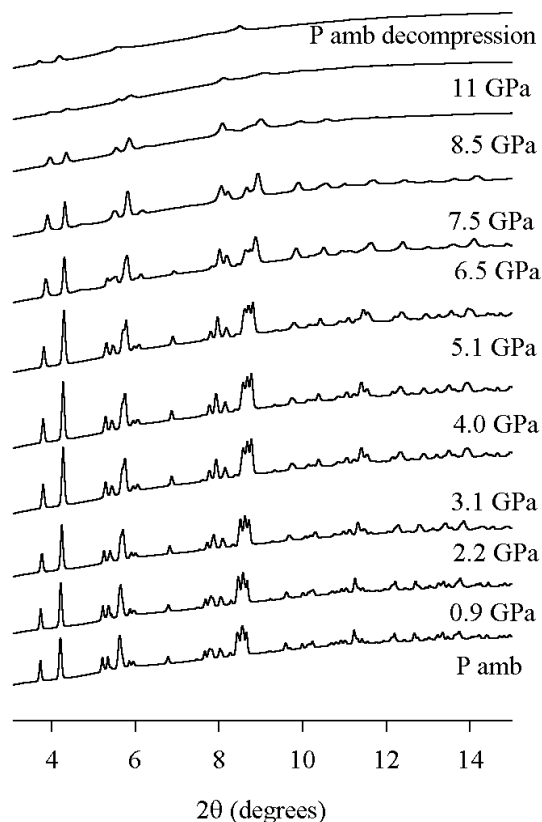

FIGURE 3. Integrated powder patterns of scolecite as a function of pressure.

TABLE 3. Lattice parameters*, volumes, and ψ angles of the systems whose atomic structures have been simulated by DF-molecular dynamics

	a (Å)	b (Å)	c (Å)	V (Å³)	ψ† comp. (°)
SCOL+	18.779	19.258	6.526	$V+$ = 2360	
SCOL	18.502	18.974	6.526	V_{exp} = 2290	19.3
SCOL1	18.317	18.784	6.526	$V1$ = 2244	19.9
SCOL2	18.132	18.594	6.526	$V2$ = 2200	21.6
SCOL3	17.947	18.404	6.526	$V3$ = 2155	23.3
SCOL4	17.762	18.215	6.526	$V4$ = 2111	23.9
SCOL5	17.577	18.025	6.526	$V5$ = 2067	24.2
SCOL6	17.392	17.835	6.526	$V6$ = 2024	24.9
SCOL7	17.207	17.645	6.526	$V7$ = 1981	25.1
SCOL8	17.577	18.025	6.395	$V8$ = 2025	24.7
SCOL9	17.577	18.025	6.265	$V9$ = 1984	25.7
SCOL8'	17.577	18.025	6.395	$V8'$ = 2025	
SCOL5'	17.577	18.025	6.526	$V5'$ = 2067	

* $\beta = 90.615°$ for all the calculations.
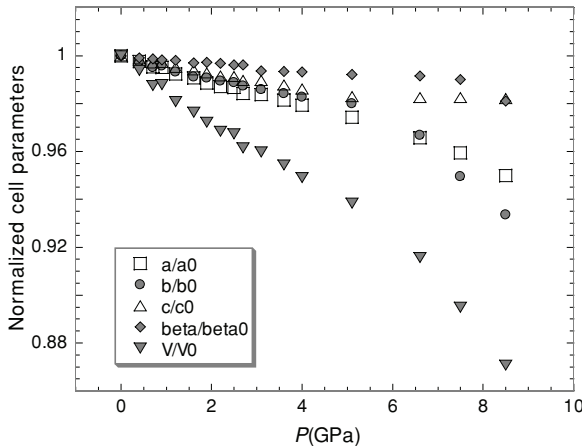† Calculated on the basis of the atomic positions obtained by the theoretical simulations.

FIGURE 4. Experimental unit-cell parameters, normalized to room condition values, vs. pressure. The errors on the cell parameters are smaller than the symbols used.

contraction is about 13%. It is worth noting that below 5 GPa a and b decreased by nearly the same amount, while at higher pressure b reduces more than a. As a consequence, the scolecite structure becomes more tetragonal at higher pressure; $b - a = 0.487$ and 0.129 at room pressure and 8.5 GPa, respectively. Figure 4 shows discontinuities in the linear pressure-dependence of the cell parameters: in particular, the slope relative to c strongly decreases at 5 GPa, while those of a and b increase at about 6.5 GPa. As a consequence, an increase in the slope of the linear pressure-volume dependence is observed just above 6 GPa, indicating a slight increase in compressibility with pressure. Miletich (2000) observed a similar behavior for gillespite-type phases and Hazen (1983) for zeolite 4A.

The mean axial compressibility of the a, b, and c axes, obtained by linear fits up to 5 GPa, are: $\beta_a = 5.0(3)10^{-3}$, $\beta_b = 3.9(3) 10^{-3}$, and $\beta_c = 3.4(2) 10^{-3}$ GPa^{-1}. The isothermal bulk modulus K_0 and its pressure derivative K_0' were fitted with a third-order Birch-Murnaghan equation of state (Birch 1952) and the values obtained were 61(2) and 9(1), respectively.

Belitsky et al. (1992) performed a HP experiment on natrolite, the Na-term with NAT topology, up to 5 GPa. The measured cell volume contraction (~5%) is only slightly lower than that found here for scolecite at the same pressure (~6%), the highest value for scolecite being justified by the different interactions of Ca, instead of Na, with framework O atoms. Moreover, the same authors did not observe any phase transitions with non-penetrating liquids, either in natrolite or in scolecite.

During the in situ HP experiments, some powder patterns of scolecite were also recorded during sample decompression. The pattern of scolecite compressed at 11 GPa and then recovered at room pressure, shown at the top of Figure 3, clearly shows that the amorphization process is irreversible upon decompression.

ATOMISTIC INTERPRETATION OF THE DEFORMATION MECHANISM

Experimental data on the thermal behavior of zeolites with NAT topology (Alberti and Vezzalini 1983; Baur and Joswig

1996) and the cell parameters determined in this work (Table 1) show that this framework is more flexible in the a-b plane than along the **c** direction, because of the high compressibility of the channels. For this reason, in our computation we applied a non-hydrostatic compression, and studied how energy increases and the atomic positions relax upon reducing the a and b lattice parameters at fixed c and b/a, for the seven unit-cell volumes ($V1$–$V7$) listed in Table 3. A unit cell with slightly expanded a and b dimensions was also investigated ($V+$) in order to improve the accuracy of our computational determination for the room pressure unit-cell volume. Next, beginning with a system already compressed along a and b ($V5$), we progressively reduced the c parameter (volumes $V8$ and $V9$) to simulate the system behavior under c compression. Finally, we tested the reversibility of the observed structural changes along two different paths: (1) by re-expanding a and b starting from $V6$ and going to V_{exp}; (2) by re-expanding c starting from $V9$ (volumes $V8'$–$V5'$ in Table 3). The angles defining the unit cell were kept fixed at their room pressure values ($\alpha = \gamma = 90°$, $\beta = 90.615°$). An additional computation (not listed in the Tables) was performed with the experimental lattice parameters at $P = 7.5$ GPa. The atomic positions computed for this last sample are fully in line with what could have been expected on the basis of the results for the successive deformations in the a-b plane and along **c**, thus confirming that these two deformation paths provide the relevant information for modeling the structural relaxation of scolecite under pressure.

The reliability of DF approximation in predicting the scolecite structure can be evaluated by comparing the computational and experimental results at room-pressure volume (Stuckenschmidt et al. 1997; Kvick et al. 1985: labeled ST and KSS, respectively, in the following text and Tables). In Table 4, we see that the mean framework bond distances and angles are predicted with an accuracy of better than ~1% and within ~4°, respectively. The most relevant discrepancies concern the hydrogen atoms (Table 5), especially with respect to the X-ray refinement results, which are affected by significant experimental uncertainties.

STRUCTURAL TRANSITIONS

The results in Figure 4 show that system compressibility increases upon increasing the applied pressure beyond ~6 GPa. This suggests that the system undergoes a structural transformation, whose details, unfortunately, are not directly accessible from our experimental measurements. Here we propose an interpretation of this behavior on the basis of the computational results. The computed total energies per atom as a function of volume under compression of the a-b basis at fixed c are displayed in Figure 5. It is apparent that these energies lie on two different, nearly parabolic curves ($E^{[i]}[V] = E^{[i]}_0 + B^{[i]} [V - V_0^{(i)}]^2$, $i = 1,2$), the lowest ($i = 1$) having $V_0^{(1)} = 2408$ Å^3 and curvature $B = 138$ GPa, the upper curve ($i = 2$) having $V_0^{(2)} = 2360$ Å^3 and $B = 65$ GPa. The absolute energy minimum at $V_0^{(1)} = 2408$ Å^3 identifies the computational ground state structure, whose lattice parameters are ~1.5% greater than the experimental ones. Moreover, the corresponding curvature $B = 138$ GPa is directly comparable to the experimental value for the inverse of the in-plane axial compressibility $1/[\beta(a) + \beta(b)] =$

TABLE 4. Framework geometrical parameters [bond distances (angstroms) and angles (°)] for the experimentally derived (Stuckenshmidt 1997) and selected computational (corresponding to different cell volumes) structures of scolecite

V(Å³)	ST 2290	SCOL 2290	SCOL1 2244	SCOL2 2200	SCOL3 2155	SCOL4 2111	SCOL5 **2067**	SCOL8 **2025**
Si1-O	1.6176	1.629	1.626	1.631	1.636	1.636	1.637	1.632
Si2-O	1.6209	1.624	1.621	1.626	1.631	1.629	1.629	1.624
Si20-O	1.6203	1.629	1.627	1.629	1.632	1.627	1.629	1.624
Al1-O	1.7494	1.743	1.738	1.743	1.749	1.746	1.745	1.740
Al10-O	1.7434	1.745	1.741	1.769	1.779	1.781	1.786	1.778
Si1-O1-Al1	134.7	130.5	128.7	132.8	130.4	130.0	129.4	127.5
Si1-O10-Al10	143.9	141.5	141.9	137.7	138.6	137.3	136.1	135.7
Si2-O2-Al1	133.1	137.1	136.4	135.6	135.1	134.1	133.3	133.1
Si20-O20-Al10	138.2	142.0	141.7	146.2	143.4	143.1	142.3	142.9
Si20-O3-Al1	135.1	135.9	135.2	135.5	135.7	135.1	134.7	133.8
Si2-O30-Al10	134.2	129.7	129.2	129.9	130.9	129.6	129.7	128.4
Si2-O4-Al1	127.6	126.6	125.6	121.6	121.6	121.3	119.5	119.8
Si20-O40-Al10	133.3	127.8	126.0	121.0	120.2	119.0	116.7	116.7
Si1-O5-Si2	151.1	146.9	145.5	143.0	142.6	141.6	139.7	138.6
Si1-O50-Si20	134.1	129.6	128.9	124.2	122.2	121.1	120.4	118.5
mean	136.5	134.8	133.9	132.7	132.1	131.2	*130.2*	*129.5*

TABLE 5. Water system geometrical parameters (distances in angstroms and angles in degrees) of the scolecite experimental and computational structures (corresponding to selected cell volumes)

V(Å³)	ST 2290	KSS 2279	SCOL 2290	SCOL1 2244	SCOL2 2200	SCOL3 2155	SCOL4 2111	SCOL5 2067	SCOL8 2025
O6— H61	0.81(5)	0.976(1)	0.99	0.99	1.00	0.99	0.98	0.98	0.98
— H62	0.89(4)	0.964(2)	0.99	0.99	0.98	0.98	0.98	0.98	0.98
H61—O6—H62	126(4)	107.3(2)	108	107	106	108	107	107	107
O6 - - - O1	2.729(1)	2.720(1)	2.67	2.66	2.65	2.75	2.76	2.77	2.76
- - - O30	3.083(1)	3.046(1)	2.79	2.76	3.04				
- - - O1						3.06	2.87	2.83	2.78
- - - O50							2.76	2.66	2.61
H61 - - - O1	1.97(4)	1.746(1)	1.68	1.67	1.65	1.77	1.78	1.80	1.79
- - - O50							1.78	1.68	1.63
H62 - - - O30	2.26(4)	2.101(2)	1.81	1.79	2.07				
- - - O1						2.11	1.90	1.87	1.82
O6—H61——O1	157(5)	177.1(2)	175	175	178	169	168	171	169
O6—H61——O50							170	176	175
O6—H62——O30	154(3)	166.1(1)	169	169	171				
O6—H62——O1						166	169	168	168
O60 — H601	0.72(4)	0.967(2)	0.98	0.98	0.99	0.99	0.99	0.99	0.99
— H602	0.83(6)	0.971(2)	0.99	0.99	1.00	1.00	1.00	1.00	1.00
H601—O60—H602	112(5)	106.6(2)	107	107	107	107	106	107	107
O60 - - - O50	2.801(1)	2.785(1)	2.76	2.74	2.73	2.79	2.78	2.79	2.79
- - - O40	3.078(1)	3.046(1)	2.74	2.73	2.76	2.79	2.78	2.75	2.73
- - - O7					2.74	2.75	2.75	2.69	2.68
- - - H72					1.74	1.76	1.75	1.69	1.68
H601 - - - O50	2.18(4)	1.828(2)	1.79	1.78	1.75	1.80	1.80	1.81	1.81
H602 - - - O40	2.52(5)	2.119(2)	1.76	1.75	1.76	1.80	1.78	1.76	1.73
O60—H601——O50	146(4)	168.5(2)	166	163	169	170	170	170	169
O60—H602——O40	125(4)	160.0(2)	168	170	177	177	177	178	177
O7 — H71	0.82(3)	0.969(1)	0.98	0.98	0.98	0.99	1.00	1.00	1.00
— H72	0.83(4)	0.950(2)	0.98	0.97	1.00	1.00	1.00	1.01	1.01
— Al2	> 3		> 3	>3	2.34	2.20	2.15	2.06	2.07
H71— O7— H72	109(3)	111.1(1)	108	107	107	108	108	109	109
O7 - - - O5	2.775(1)	2.756(1)	2.71	2.67					
- - - O10	2.676(1)	2.657(1)	2.68	2.66					
- - - O30					3.18	3.00	2.93	2.88	2.89
- - - O60					2.74	2.75	2.75	2.69	2.68
H71 - - - O5	2.20(3)	2.038(2)	1.85	1.75					
- - - O30					2.20	2.02	1.96	1.89	1.81
H72 - - - O10	1.92(3)	1.770(1)	1.94	2.08					
- - - O60					1.74	1.76	1.75	1.69	1.68
O7— H71——O5	127(3)	130.9(1)	144	153					
O7— H71——O30					176	171	172	172	171
O7— H72——O10	153(3)	150.5(1)	130	117					
O7— H72——O60					172	170	170	170	169

Notes: ST = Stuckenshmidt et al. (1997); KSS = Kvick et al. (1985).
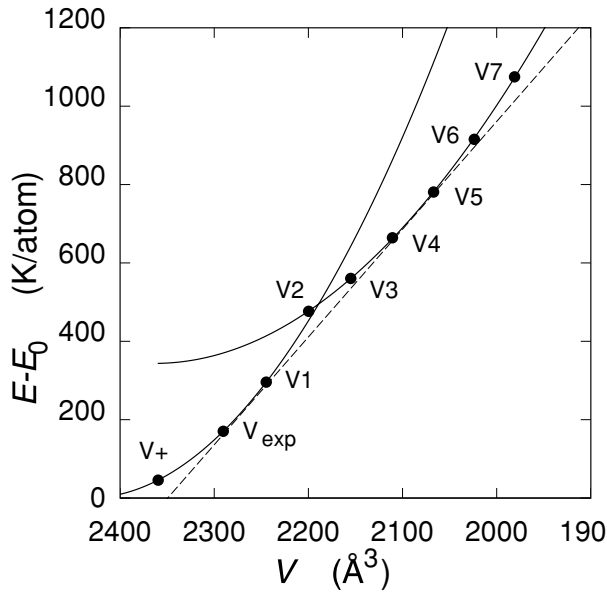
FIGURE 5. Total energy from DF computations vs. unit-cell volume upon compressing the *a-b* lattice parameters at fixed *c*. E_0 is the computed ground state energy. Dots = DF computations at the lattice parameters listed in Table 3. Full lines = parabolic fit for the low- and high-density portions of the computed points. Dashed line = common tangent to the parabolic interpolations.
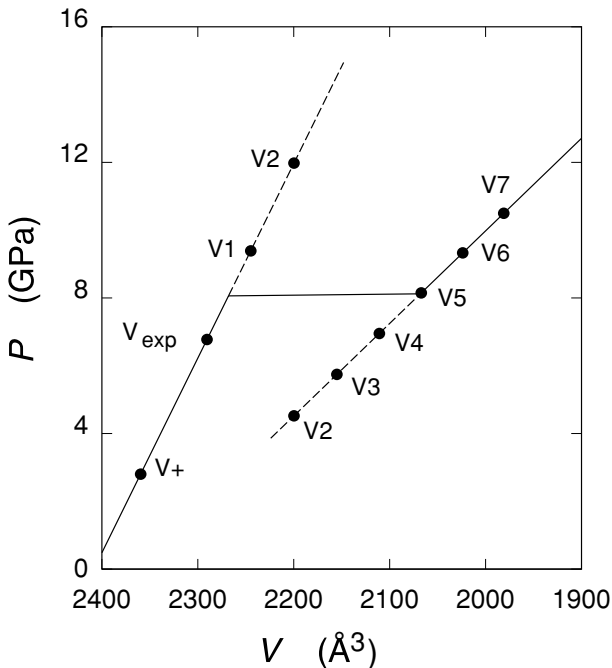

FIGURE 6. Pressure vs. unit-cell volume from DF computations. Dots = DF computations at the lattice parameters listed in Table 3. Straight lines = volume derivative of the parabolic fits shown in Figure 5. The horizontal line corresponds to the common tangent to the parabolas. The equilibrium $P(V)$ relation is identified by the full line. Dashed lines represent metastable conditions.

110 GPa. These discrepancies for both the lattice constant and for the inverse compressibility are in line with the accuracy obtained in recent studies for simpler silicates (Hamann 1996) using computational methods equivalent to ours.

The two curves intersect at $V = 2200$ Å³, with an energy that is ~500 K above the absolute minimum. According to the rules of equilibrium thermodynamics (Callen 1985), the phase diagram of a system exhibiting two different forms is given by the convex envelope of the corresponding energy curves. If the two energies intersect each other by changing volume, the convex envelope can be determined graphically by drawing the common tangent to these curves, as shown by the dashed line in Figure 5. At volumes $V \geq V1$, therefore, the stable phase of the system corresponds to the lowest energy curve; at volumes $V \leq V4$ the system energy is represented by the upper parabola. In between ($V4 \leq V \leq V1$) the system has two coexisting phases, with the energy varying linearly between the two volumes $V4$ and $V1$. The two homogeneous phases are separated by a volume gap between $V1$ and $V4$, therefore the transition is first order. At each volume, the pressure is computed as the derivative of the system energy with respect to the volume. The results displayed in Figure 6 show that, in agreement with the experimental results reported in Figure 4, the highest density phase is more compressible than the low density one, as apparent from the lower slope of the pressure vs. volume line for $V \leq V4$. The constant pressure range at 8.1 GPa identifies the pressure of this first order transition.

Despite overestimation of the transition volume and pressure, we identify this transition with the anomaly in the experimental data at $V \sim 2100$ Å³ and $P \sim 6$ GPa. The lack of significant discontinuity in the experimental volume, which contrasts with the first order character of the transformation predicted by the computation, could be the result of rounding of the transition due to the non-zero temperature in the experimental sample. Moreover, the rules applied to predict the phase diagram from our DF computations refer strictly to thermodynamic equilibrium, while experiments on phase transitions sometimes display significant hysteresis effects, especially for solids under pressure.

We analyzed the atomistic mechanisms underlying the transition by focusing our attention on the geometry of the water molecules filling the channels, the volume and shape of the channels parallel to *c*, and the coordination of the Si, Al, and Ca cations. In the following section the atom labels are from Stuckenschmidt et al. (1997).

Hydrogen bond restructuring and channel volume

The most apparent transformation at the transition is displayed by the configuration and bonding of water molecules. The computational results for SCOL ($V_{exp} = 2290$ Å³) show that each water hydrogen atom is engaged in a hydrogen bond with a framework O atom. These bonds, however, are not equally strong. Judging from geometrical parameters (Table 5), the water molecule O6 forms one strong and one weak bond with the framework; O60 has two equally strong bonds, while the two O7 bonds are characterized by fairly long bond distances, and far from linear O-H—O angles ($\theta = 130°$ and $144°$, respectively). These results are in quite close agreement with the experimental data reported by Kvick et al. (1985) with, however,

some quantitative differences: the hydrogen bonds appear to be better defined in the computation than in the experimental results, and the spread in the water intra-molecular HOH angles (107–108°) given by our computation is narrower than in the experiment (106.6–111.1°). Upon reducing a and b, the beginning of the transition ($V1 = 2244$ Å³) is marked by further lengthening of the longest H-bond of O7 (2.08 Å), while the shorter bond becomes better defined (1.75 Å). At $V2 = 2200$ Å³ we observe the formation of a strong water-water hydrogen bond (2.74 Å), with O7 as donor and O60 as the acceptor. The dimer formation is also accompanied by rotation of the water molecule O7, which was approximately in the a-b plane, out of the plane by about 90°. Starting from this volume, this intra-water bond remains the most stable and best defined hydrogen bond in the system. It is tempting to propose this restructuring of the water bonding as the driving force for the transition. It is worth noting that the restructuring of the water bonding does not affect the symmetry of the system (all the calculated atomic coordinates respect the $F1d1$ space group) and hence new diffraction peaks are neither expected nor observed in the experimental patterns.

With increasing pressure, we observe a few other transformations in the hydrogen bonding configuration, represented by the change in the identity of the framework O atom acceptors of the O6 and O7 water molecules (Table 5), while we do not observe the formation of additional water-water bonds. The driving force for these successive transformations in the hydrogen bonding is apparently very small, because they do not produce any detectable anomaly in the energy vs. volume curves (see Fig. 5). Therefore, during the HP experiments, and in the presence of hysteresis, it is likely that these changes do not occur simultaneously across a macroscopic crystal. As a result, they do not appear as phase transitions, but they continuously modify the macroscopic crystal properties (volume, compressibility), and, more importantly, they introduce a mechanism to disorder the system.

These observations are reflected in the pressure dependence of the volume of the channels (V_{ch}), defined as the measure of the space within the channels separated by more than 2 Å from the framework O atoms. This quantity, relative to the channel running along c and estimated by a simple Monte Carlo integration, is reported in Figure 7 as a function of the total system volume. The major discontinuity at 2200 Å³ is apparently related to the transition induced by the formation of the water dimer. The slope of V_{ch} vs. total volume V decreases slightly across the first order transition, showing that the compressibility of this channel decreases with increasing pressure, at variance from what is found (both experimentally and by the computation) for the system as a whole. More importantly, the volume of the channels contracts under pressure much faster than the total volume, as apparent from the fact that the volume fraction represented by channels decreases under compression: V_{ch} represents ~18% of the total volume SCOL, but is reduced to ~14% at $V7$. All these observations point to the hydrogen bonding network as a crucial feature affecting the channel geometry and volume. Changes in the hydrogen bonding appear as anomalies in V_{ch}, and even the high compressibility of the channels might be related to the hydrogen bonding with
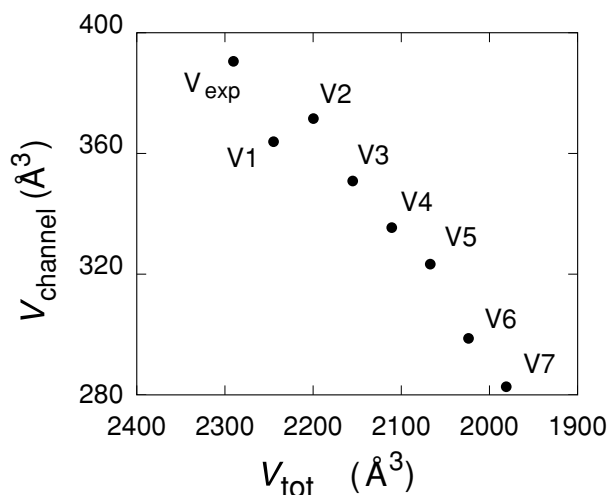

FIGURE 7. Computed free volume of the channel parallel to c as a function of the cell volume.

framework O atoms: most of these bonds appear to be slightly stretched (O—H distances $\geq$ 1.75 Å), thus providing an internal force that helps to reduce V_{ch} when external pressure is applied to the system. This interpretation is supported by the observation that, upon breaking the water-framework hydrogen bond to form the water dimer (see SCOL2 in Table 5), V_{ch} expands by ~2% (Fig. 7), although the external pressure increases.

Evolution of the tetrahedra geometry

The general effect of compression on the scolecite framework is shown in Table 4, where the mean T-O bond distances and T-O-T bond angles are reported for selected computed structures, and in Figure 8, where the tetrahedra volumes are reported for the simulations up to SCOL7, regarding the structures compressed in the a-b plane. We observe that, while the T-O bond lengths remain remarkably constant down to the smallest volumes, the T-O-T mean angles decrease from 136.5° in SCOL to 129.5° in SCOL8. This trend is in very close agreement with the one inferred by Gillet et al. (1996) for scolecite on the basis of Raman frequency measurements, and similar T-O-T bond-angle changes were also observed in SiO_2 and GeO_2 quartz prior to amorphization (Hazen et al. 1989; Madon et al. 1991).

In SCOL, the tetrahedra Si1, Si2, and Si20 have almost ideal geometry and equal volume. Their evolution with increasing pressure (Fig. 8) is qualitatively similar, with only slight quantitative differences. At first, the volumes of the three tetrahedra decrease slowly with increasing pressure. At the transition, however, they all relax outward, recovering the volume lost in the initial compression. For volumes $V \leq V4$, the three tetrahedra display slightly different compressibilities, Si1 being the least compressible of the three. As a result of the non-monotonic changes upon reducing the total volume, the silicon tetrahedra appear to be far less compressible than the unit cell as a whole: in going from SCOL to SCOL7, the total volume is reduced by more than 13%, while the silicon tetrahedra reduce their volume by 1.5% at most. It is worth mentioning that below $V = 2111$ Å³, the eight tetrahedra of the unit cell are no longer equivalent, and display an increasing deviation from

*F*1*d*1 symmetry with increasing pressure. This deviation is, however, quantitatively too small to be detected in the experimental data (about ±0.006 on the fractional coordinates). We again emphasize that most changes described above for the SiO$_4$ tetrahedra come from changes in the O-Si-O angles, while the Si-O bond length remains nearly constant down to the smallest volumes investigated (Table 4).

With increasing pressure, the Al1 tetrahedron displays volume changes similar to those of silicon (Fig. 8), resulting in a very low net volume change [ΔV(Al1)/V(Al1) ~1% from SCOL to SCOL7]. The behavior of Al10 is different, in that its coordination tetrahedron shows a nearly monotonic decrease in volume with increasing pressure. Moreover, by analyzing the atomic positions, we observe the progressive penetration in the coordination sphere of an additional water O atom (O7) that reaches a distance of ~2 Å in SCOL5 (Table 4), thus raising the formal coordination of Al10 from four to five. This is not the first time that a similar coordination is observed in zeolites; a fivefold framework site forms during the heating-induced phase

transformation of brewsterite (Alberti et al. 1999; Sacerdoti et al. 2000), accompanying the T-O-T breaking of the framework. However, in the case of scolecite, a closer look at O-Al10-O angles (which are close to 90°), shows that the shape of the Al10 coordination polyhedron is actually transformed from tetrahedral to octahedral, with the intervention of a sixth O atom whose distance from Al10 (2.79 Å in SCOL7) is very long but rapidly decreasing. Despite these peculiar features, the relative volume change of the Al10 tetrahedron [ΔV(Al10)/V(Al10) ~8%, from SCOL to SCOL7, computed by considering only the O atoms coordinating Al10 in SCOL, and excluding the incoming O atoms] is again lower than the change in the total cell volume. The Si and Al tetrahedra, therefore, behave like almost rigid units under pressure, justifying the common view of these tetrahedra as the natural building blocks for these framework systems.

Evolution of Ca coordination

The response of the Ca coordination to increasing pressure is similar to that of the Si and Al tetrahedra (Fig. 8). The geometry of the Ca polyhedron at different cell volumes is displayed in Figure 9. Figure 10 shows the corresponding variation of Ca coordination number as a function of distance. At low pressure, the O atom coordination of Ca can be described as forming a deformed pentagonal bipyramid, whose seven vertices are provided by four framework O atoms and three O atoms of water molecules (Fig. 9a). With decreasing volume, the O-Ca-O angles gradually change, while the O-Ca distances remain constant. The volume of the bipyramid coordinating Ca is reduced at a relative rate nearly equal to that of the total system volume (Fig. 8). The formation of the water-water hydrogen bond at V2, involving two of the O atoms coordinating Ca, has a small but detectable effect on the geometry of the pentagonal bipyramid. With decreasing *a* and *b*, the volume of the Ca polyhedron continues to shrink monotonically and almost linearly, with an apparent compressibility that is slightly less than in the low pressure phase (Fig. 8). More importantly, we observe the progressive penetration of an additional framework O atom into the Ca coordination shell, reaching a distance of about 3.1 Å for SCOL5 (curve b in Fig. 10), and 2.9 Å for SCOL7. This distance is close to (but still longer than) the average Ca-O distance of 2.6 Å for the seven O atoms coordinating calcium at low pressure. We emphasize that this mean distance, characterizing the sevenfold inner coordination of Ca, remains remarkably constant during the entire compression of the *a-b* plane, while the corresponding O-Ca-O angles display larger and sometimes almost discontinuous changes (Fig. 9).

Evolution of the coordination polyhedra upon reducing *c*

Interestingly, but not unexpectedly, the structural transformations induced by squeezing along the *c* axis are qualitatively different from those induced by reducing *a* and *b*, as we verified by analyzing the atomic structure for volumes V8 and V9. The most important effect of reducing *c* is an expansion of the inner coordination shell of Ca from V8 to V9 (Fig. 9c and curve **c** in Fig. 10). This counter-intuitive outward relaxation with increasing pressure points to an incipient structural instability taking place at pressures beyond 10 GPa.
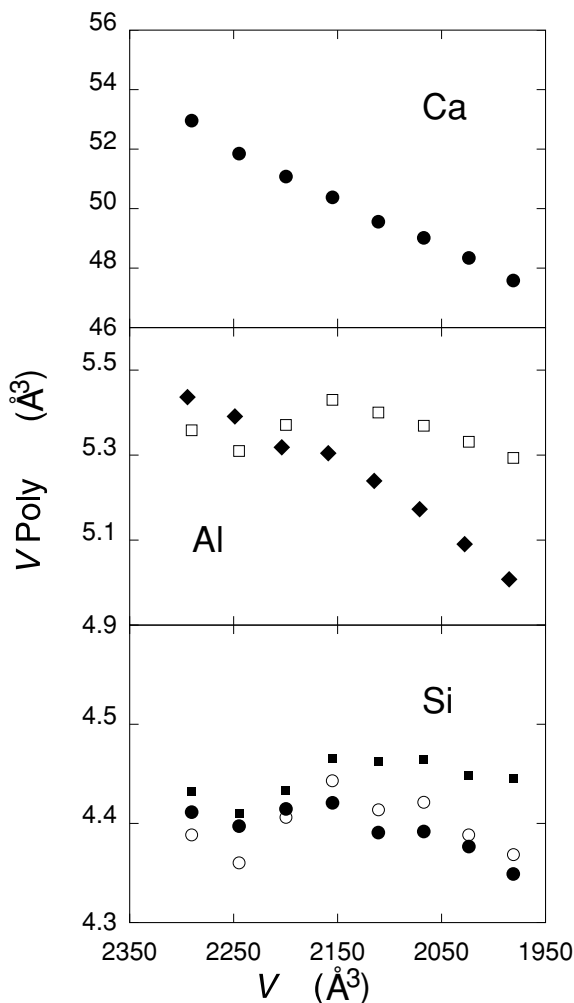

FIGURE 8. Dependence of Si (Si1 = filled square, Si2 = open circle, Si20 = filled circle), Al (Al1 = open square, Al10 = filled diamond) and Ca coordination polyhedron volumes on the unit-cell volume. The reported data regards the simulations from SCOL to SCOL7.
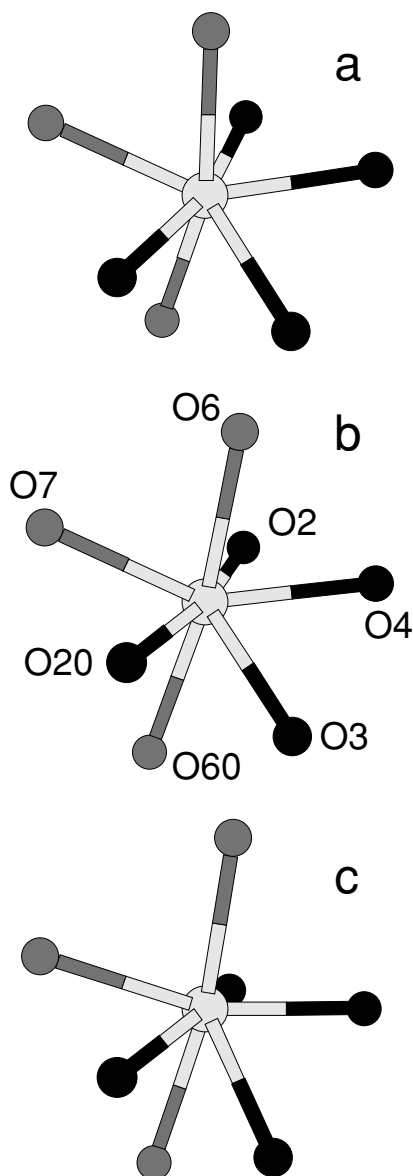
FIGURE 9. Geometry of calcium coordination polyhedron in (**a**) SCOL, (**b**) SCOL5, and (**c**) SCOL9. The framework O atoms are drawn in black, those of the water molecules in gray.
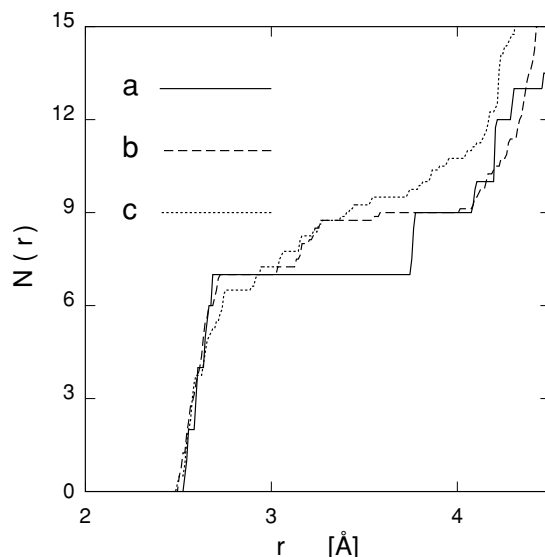

FIGURE 10. Average coordination number of Ca vs. distance at three different cell volumes: (**a**) SCOL, (**b**) SCOL5, and (**c**) SCOL9.

The effect of reducing c on the Si and Al coordination is also quantitatively important, but less easy to interpret than for Ca. In the case of Si, reducing c from $V5$ to $V8$ significantly decreases the volume of all the tetrahedra, but this trend does not continue (and it even shows signs of reversing) from $V8$ to $V9$. Al1 displays the same behavior. The effect on Al10 is, once again, different, since reducing c partially reverses the pressure evolution in its polyhedron bond lengths and angles, observed during compression along a and b. In particular, the distance between Al10 and the sixth approaching O atom becomes larger than 3 Å and the internal angles of the Al10 polyhedron increase. The structural deformations described in this section, which occur at cell volumes lower than those experimentally investigated, produce a symmetry lowering to the space group $A111$, caused mainly by disorder in the Ca coordination.

PRESSURE-INDUCED AMORPHIZATION

The band broadening observed in the X-ray patterns with increasing pressure indicates, in agreement with the Raman and X-ray diffraction data of Gillet et al. (1996), a progressive long-range disordering in the scolecite structure, preceding the transition to the amorphous phase. Again in agreement with these authors, the crystal-to-amorphous transition is irreversible upon decompression, as shown by the powder patterns in Figure 3. This irreversibility is compatible with the fact that the HP-induced structural modifications in scolecite are not elastic deformations, but reflect real chemical bonding changes in parts of the structure (Yamanaka et al. 1997).

Our DF computations cannot provide a direct view of the amorphization process, which involves many different length scales, as they are limited to a very short length scale (one unit cell). We may, nevertheless, use DF calculations to investigate the atomistic features that imply the presence of disorder on the macroscopic scale. We focus, in particular, on the irreversibility of the structural deformations under compression, which points unambiguously to the presence of multiple local minima in the system potential energy surface. In our computation, irreversible phenomena manifest themselves both in the atomic coordinates and in the total energy, which, upon decompression, remains above the original energy at the same volume before compression. We identify two different phenomena. The first is irreversibility in the hydrogen bonding structure, which produces a very minor degree of irreversibility in the framework. Because of the well known limitations of X-ray diffraction in detecting hydrogen positions from HP data, this form of irreversibility is difficult to detect experimentally. The second form is an intrinsic irreversibility in the framework that is much more apparent in the experimental data (Fig. 3). Not surprisingly, the first form of irreversibility appears at moderate pressure, as verified by reversing compression from $V6$ to V_{exp} (SCOL). The longest structural relaxation allowed by our simulation method (corresponding to several picoseconds in real

time) does not restore the original pattern of hydrogen bonds. The water dimer, in particular, does not break easily, despite its prompt formation during compression. In the same pressure-volume range (up to V5), deformations of the framework appear to be much more reversible. Otherwise, apparent irreversibility in the framework arises at higher pressure, and, in particular, upon significantly reducing the *c* lattice parameter: upon re-expanding V9 to V8' and then to V5', we observe that the increase in the Al10 coordination, and the increase in the average Ca-O nearest neighbor distance, do not reverse, and even tend to become stronger. We emphasize once more that these results provide only indirect information on the amorphization process, and only a more empirical modeling, based on the present DF results and covering a wider range of length and size scales, could provide a more direct view. Nevertheless, the combination of the experimental and computational results suggests that amorphization could take place through the following steps: formation of a water dimer, its approach to a framework Al10 atom, resulting in a fivefold coordination of the cation, and, finally, modification of the Ca coordination shell. The coordination change of the Al cation, in particular, could be the causative step for the opening of that tetrahedron, and for the T-O-T bridge breaking.

SIMPLE GEOMETRICAL MODELS OF THE HP FRAMEWORK DEFORMATIONS AND COMPARISON WITH THE HT BEHAVIOR

Previous studies performed on natrolite (Alberti and Vezzalini 1981, 1983; Baur et al. 1990; Joswig and Baur 1995; Baur and Joswig 1996) evidenced a relationship between the cell parameters of natural, dehydrated, and ion-exchanged natrolite, and a number of geometrical features of the framework. Specifically, heating natrolite causes dehydration of the mineral and a consequent strong contraction of cell volume and channel dimensions. These heating-induced framework deformations are achieved through two main mechanisms: (1) rotation of the tetrahedral chain around its axis (ψ angle), producing a decrease of *a* and *b* parameters; (2) rotation of each tetrahedron (α angle) around an axis perpendicular to *c*, causing a twisting of the chain and a decrease of the *c* parameter. The rotation angle ψ can be calculated from the cell parameters following the formulae reported by Alberti and Vezzalini (1981), based on geometrical features of natrolite structure. In this work we observed the effect of pressure on the cell parameters of the NAT topology Ca-term. Since we also observed a contraction of the cell volume, we tentatively assumed that the deformation mechanism is similar to that observed during fibrous zeolite dehydration. Therefore, we calculated, on the basis of the experimental cell parameters and of the formulae reported by Alberti and Vezzalini (1981), the ψ values at different pressures (Table 1), assuming that the tetrahedra are incompressible and taking the mean values of the Si-O and Al-O distances from the most recent scolecite structural refinement (Stuckenschmidt et al. 1997).

The atomic positions resulting from the DF computations in this work provide a unique opportunity to test the validity of this simple model. Needless to say, the slight differences in bond distances and angles between experimental and computed

structures imply that a model calibrated on either experiments or computations cannot quantitatively fit both sets of data. For this reason, we focus our analysis on the angle variations under pressure, rather than on their absolute values.

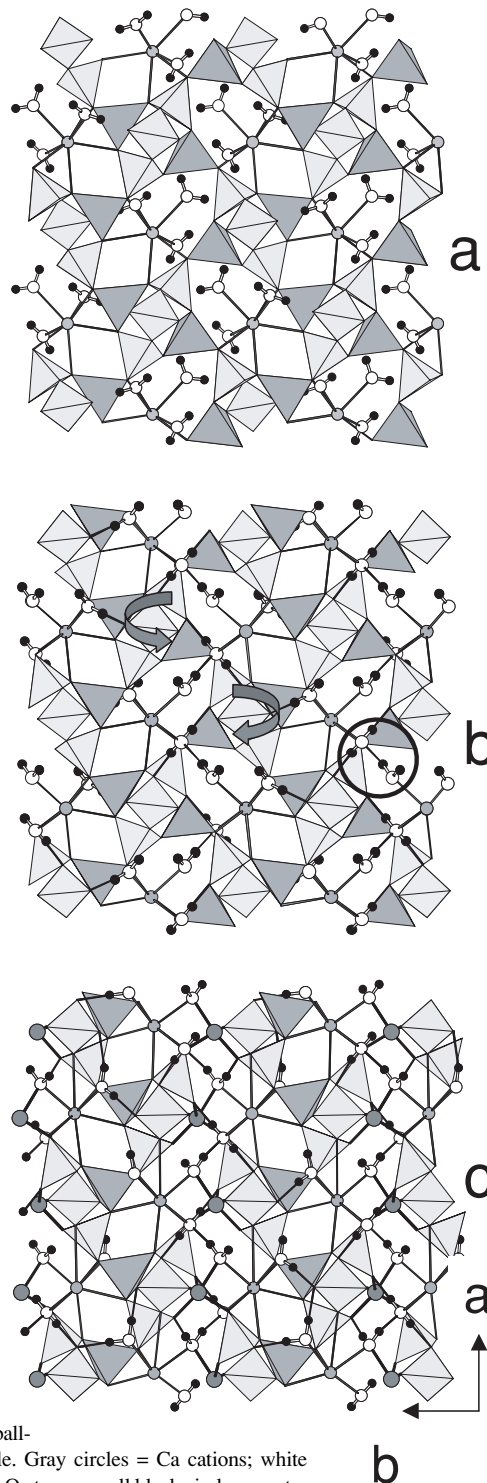Figures 11a–c show projections along the *c* axis of the struc-

FIGURE 11. Selected scolecite computed structures viewed on the *ab* plane: (**a**) SCOL; (**b**) SCOL2; (**c**) SCOL5. In SCOL2 the curved arrows indicate the rotation induced by pressure on the tetrahedral chains running along *c*; the water dimer is also highlighted. In SCOL5 the A 1 1 0 polyhedron is shown in the "ball-and-stick" style. Gray circles = Ca cations; white circles = water O atoms; small black circles = water hydrogens; large gray circles = Al cations.

ture of scolecite simulated at different cell volumes (SCOL, SCOL2, and SCOL5). In the structure shown in Figure 11b, the water dimer is already formed, while Figure 11c also shows the fivefold coordinated aluminum atom Al10 in the "ball-and-stick" style. It is evident that the contraction of the a and b parameters induces the rotation in the a-b plane of the tetrahedral chains and causes a strong compression of the channel. This deformation is facilitated by the observed rotation of the O7 water molecule outside the a-b plane during the water dimer formation. The value of the ψ angle, determined on the basis of the calculated atomic positions (ψ_{comp} in Table 3), increases

from 19.3° to 25.7° from SCOL to SCOL9. The $\Delta\psi_{comp}$ is 6.4°, in good agreement with that calculated following the method developed for natrolite by Alberti and Vezzalini (1981), using the values of the experimental cell parameters, from room pressure up to 8.5 GPa (ψ_{cell} in Table 1; $\Delta\psi_{cell}$ = 7.2°). Differences are observed in the absolute values of the rotation angle determined by the two methods. This can be explained by the presence in the formulae proposed by Alberti and Vezzalini (1981) of a geometrical term reflecting the twisting of the tetrahedra in the chain running parallel to c. This twisting is greater in scolecite than in natrolite at room pressure (see Figs. 12a and 12b).

Figure 12 also shows a comparison between the configuration of the tetrahedral chain of scolecite simulated at different cell volumes (SCOL, SCOL2, and SCOL9). SCOL and SCOL2 differ in a and b cell parameters, while SCOL9 is also characterized by a 4% contraction of the c parameter. We observe an increase of the α angle, causing a twisting of the chain, due to the pressure-induced rotation of the tetrahedra around an axis perpendicular to c. As a conclusion, these results confirm that, on the whole, the response of the fibrous zeolitic frameworks to high-T or high-P solicitation follows similar deformation mechanisms.

FIGURE 12. Comparison between the configurations of the tetrahedral chain of (**a**) natrolite and those computed for (**b**) SCOL, (**c**) SCOL2, (**d**) SCOL9.

REFERENCES CITED

Alberti, A. and Vezzalini, G. (1981) A partially disordered natrolite: relationships between cell parameters and Si-Al distribution. Acta Crystallographica, B37, 781–788.
——— (1983) How the structure of natrolite is modified through the heating-induced dehydration. Neues Jahrbuch für Mineralogie Monatshefte, 1983, 3, 135–144.
——— (1984) Topological changes in dehydrated zeolites: Breaking of T-O-T bridges. In D. Olson and A. Bisio, Eds., Proceedings of the 6th International Zeolite Conference, Reno, 1983, p. 834–841. Butterworths, Guildford, United Kingdom.
Alberti, A., Sacerdoti, M., Quartieri, S., and Vezzalini, G. (1999) Heating-induced phase transformation in zeolite brewsterite: new 4- and 5-coordinated (Si, Al) sites. Physics and Chemistry of Minerals, 26, 181–186.
Baur, W.H. and Joswig, W. (1996) The phases of natrolite occurring during dehydration and rehydration studied by single-crystal X-ray diffraction methods between room temperature and 923 K. Neues Jahrbuch für Mineralogie Monatshefte, H.4, 171–187.
Baur, W.H., Kassner, D., Kim, C.-H., and Sieber, N.H.W. (1990) Flexibility and distortion of the framework of natrolite: crystal structure of ion-exchanged natrolites. European Journal of Mineralogy, 2, 761–769.
Bazhan, I.S., Kholdeev, O.V., and Fursenko, B.A. (1999) Phase transformations in scolecite at high hydrostatic pressure. Doklady Akademy Nauk, 364, 97–100 (in Russian).
Belitsky, I.A., Fursenko, B.A., Gabuda, S.P., Kholdeev, O.V., and Seryotkin Yu.V. (1992) Structural transformations in natrolite and edingtonite. Physics and Chemistry of Minerals, 18, 497–505.
Birch, F. (1952) Elasticity and constitution of the earth's interior. Journal of Geophysical Research, 57, 227–286.
Bish, D.L. (1995) Thermal behavior of natural zeolites. In D.W. Ming and F.A. Mumpton, Eds., Natural Zeolites '93, p. 259–269. Brockport, New York.
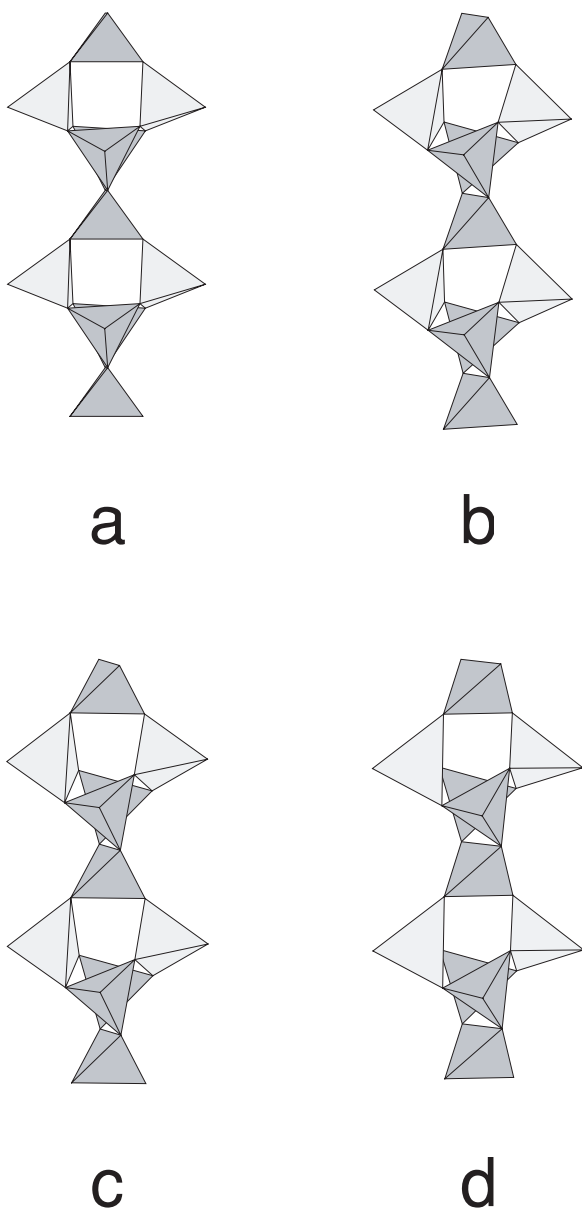Callen, H.B. (1985) Thermodynamics and an introduction to thermostatics. Wiley, New York.

Car, R. and Parrinello, M. (1985) Unified approach for molecular dynamics and density-functional theory. Physical Review Letters, 55, 2471–2474.

Comodi, P., Gatta, G. D., and Zanazzi, P.F. (2001) High-pressure structural behavior of heulandite. European Journal of Mineralogy, 13, 497–505.

Fälth, I. and Hansen, S. (1979) Structure of scolecite from Poona, India. Acta Crystallographica, B35, 1877–1880.

Finger, L.W., Cox, D.E., and Jephcoat, A.P. (1994) A correction for powder diffraction peak asymmetry due to axial divergence. Journal of Applied Crystallography, 27, 892–900.

Galli, G. and Parrinello, M. (1991) Computer Simulations in Material Science, In M. Meyer and V. Pontikis, Eds., NATO ASI Series E: Applied Sciences, 205, p. 283–304. Kluwer, Dordrecht.

Gillet, P., Malézieux, J.M., and Itiè, J.P. (1996) Phase changes and amorphyzation of zeolites at high pressures: the case of scolecite and mesolite. American Mineralogist, 81, 651–657.

Goryainov, S.V., Fursenko, B.A., and Belitsky, I.A. (1996) Phase transitions in analcime and wairakite at low-high temperatures and high pressure. Physics and Chemistry of Minerals, 23, 297–298.

——— (1999) Raman spectroscopy of phase transition and amorphyzation of wairakite at high pressure. Doklady Akademy Nauk, 369, 70–73.

Hamann, D.R. (1996) Generalized gradient theory for silica phase transitions. Physical Review Letters, 76, 660–663.

——— (1997) H_2O hydrogen bonding in density-functional theory. Physical Review B, 55, 10157–10160.

Hammersley, A.P., Svensson, S.O., Hanfland, M., Fitch, A.N., and Häusermann, D. (1996) Two-dimensional detector software: from real detector to idealized image or two-theta scan. High Pressure Research, 14, 235–248.

Hazen, R.M. (1983) Zeolite molecular sieve 4A: anomalous compressibility and volume discontinuity at high pressure. Science, 219, 1065–1067.

Hazen, R.M. and Finger, L.W. (1979) Polyhedral tilting: a common type of pure displacive phase transition and its relationship to analcite at high pressure. Phase Transitions, 1, 1–22.

——— (1984) Compressibility of zeolite 4A is dependent on the molecular size of the hydrostatic pressure medium. Journal of Applied Physics, 56, 1838–1840.

Hazen, R.M., Finger, L.W., Hemley, R.J., and Mao, H.K. (1989) High-pressure crystal chemistry and amorphization of α-quartz. Solid State Communication, 72, 507–511.

Huang, Y. (1998) IR spectroscopic study of the effect of high pressure on zeolites Y, A and sodalite. Journal of Material Chemistry, 8, 1067–1071.

Hutter, J., Lüthi, H.P., and Parrinello, M. (1994) Electronic structure optimization in plane-wave-based density functional calculations by direct inversion in the iterative subspace. Computational Material Science, 2, 244–248.

Joswig, W. and Baur, W.H. (1995) The extreme collapse of a framework of NAT topology: The crystal structure of metanatrolite (dehydrated natrolite) at 548 K. Neues Jahrbuch für Mineralogie Monatshefte, H.1, 26–38.

Kvick, Å., Ståhl, K., and Smith, J.V. (1985) A neutron diffraction study of the bonding of zeolitic water in scolecite at 20 K. Zeitschrift für Kristallographie, 171, 141–154.

Larson, A.C. and Von Dreele, R.B. (1994) GSAS-General Structure Analysis System. Report LAUR 86-748, Los Alamos National Laboratory, Los Alamos, New Mexico.

Le Bail, A., Duroy, H., and Fourquet, J.L. (1988) Ab-initio structure determination of $LiSbWO_6$ by X-ray powder diffraction. Material Research Bulletin, 23, 447–452.

Le Bihan, T., Heathman, S., Darracq, S., Abraham, C., Winand, J-M., and Benedict, U. (1996) High pressure X-ray diffraction studies of UX3 (X = Al, Si, Ga, Ge, In, Sn). High Temperatures-High Pressures, 27/28, 157–162.

Lee, Y., Hriljac, J.A., Vogt, T., Parise, J.B., and Artioli, G. (2002) First structural investigation of a super hydrated zeolite. Journal of Physical Chemistry, 124, 5466–5475.

Madon, M., Gillet, Ph., Julien, C., and Price, G.D. (1991) A vibrational study of phase transitions among the GeO_2 polymorphs. Physics and Chemistry of Minerals, 19, 381–391.

Mao, H.K., Xu, J., and Bell, P.M. (1986) Calibration of the ruby pressure gauge to 800 Kbar under quasi-hydrostatic conditions, Journal of Geophysical Research, 91, 4673–4676.

Marx, D. and Hutter, J. (2000) Ab-initio molecular dynamics: theory and implementation. In J. Grotendorst, Ed., Modern Methods and Algorithms of Quantum Chemistry. John von Neumann Institute for Computing, Jülich, NIC Series, Vol. 1, p. 301–449.

Meier, W.M., Olson, D.H., and Baerlocher, Ch. (1996) Atlas of zeolite structure types. Zeolites 17, 1–229.

Miletich, R. (2000) The tetragonal-to-tetragonal phase transition in gillespite-type phases. Is there elastic softening at high pressures? VIII EMPG, Bergamo (Italy) 16-19/4/2000, p. 71.

Moroz, N.K., Kholopov, E.V., Belitsky, I.A., and Fursenko, B.A. (2001) Pressure-enhanced molecular self-diffusion in microporous solids. Microporous and Mesoporous Materials, 42, 113–119.

Perdew, J.P., Burke, K., and Ernzerhof, M. (1996) Generalized Gradient Approximation Made Simple. Physical Review Letters, 77, 3865–3868.

Sacerdoti, M., Vezzalini, G., and Quartieri, S. (2000) Dehydration mechanism in brewsterite: single-crystal X-ray diffraction study. Microporous and Mesoporous Materials, 41, 107–118.

Secco, R.A. and Huang, Y. (1999) Pressure-induced disorder in hydrated Na-A zeolite. Journal of Physics and Chemistry of Solids, 60, 999–1002.

Schulze, C., Lienert, L., Hanfland, M., Lorenzen, M., and Zontone, F. (1998) Microfocusing of hard X-rays with cylindrically bent crystal monochromators. Journal of Synchrotron Radiation, 5, 77–81.

Ståhl, K. and Hanson, J. (1994) Real-time synchrotron powder diffraction studies of the dehydration processes in scolecite and mesolite. Journal of Applied Crystallography, 27, 543–550.

Stuckenschmidt, E., Joswig, W., Baur, W.H., and Hofmeister, W. (1997) Scolecite, Part I: refinement of high-order data, separation of internal and external vibrational amplitudes from displacement parameters. Physics and Chemistry of Minerals, 24, 403–410.

Thomson, P., Cox, D.E., and Hastings, J.B. (1987) Rietveld refinement of Debye-Scherrer synchrotron X-ray data from Al_2O_3. Journal of Applied Crystallography, 20, 79–83.

Troullier, N. and Martins, J.L. (1991) Efficient pseudopotentials for plane-wave calculations. Physical Review B, 43, 1993–2006.

Velde, B. and Besson, J.M. (1981) Raman spectra of analcime under pressure, Physics and Chemistry of Minerals, 7, 96–99.

Vezzalini, G., Quartieri, S., Sani, A., and Levy, D. (2001) The structural modifications induced by high pressure in scolecite and heulandite: in-situ synchrotron X-ray powder diffraction study. Proceedings of the XIII International Zeolite Conference, Montpellier (France), July 8–13, 2001.

Yamanaka, T., Nagay, T., and Tsuchiya, T. (1997) Mechanism of pressure-induced amorphization. Zeitschrift für Kristallographie, 212, 401–410.